

Unfiltering of the Geostationary Earth Radiation Budget (GERB) Data. Part I: Shortwave Radiation

N. CLERBAUX, S. DEWITTE, C. BERTRAND, D. CAPRION, B. DE PAEPE, L. GONZALEZ, AND A. IPE

Royal Meteorological Institute of Belgium, Brussels, Belgium

J. E. RUSSELL AND H. BRINDLEY

Imperial College, London, United Kingdom

(Manuscript received 28 February 2007, in final form 4 September 2007)

ABSTRACT

The method used to estimate the unfiltered shortwave broadband radiance from the filtered radiances measured by the Geostationary Earth Radiation Budget (GERB) instrument is presented. This unfiltering method is used to generate the first released edition of the GERB-2 dataset. The method involves a set of regressions between the unfiltering factor (i.e., the ratio of the unfiltered and filtered broadband radiances) and the narrowband observations of the Spinning Enhanced Visible and Infrared Imager (SEVIRI) instrument. The regressions are theoretically derived from a large database of simulated spectral radiance curves obtained by radiative transfer computations. The generation of the database is fully described.

Different sources of error that may affect the GERB unfiltering have been identified and the associated error magnitudes are assessed on this database. For most of the earth-atmosphere conditions, the error introduced during the unfiltering process is below 1%. In some conditions (e.g., low sun elevation above the horizon) the error can present a higher relative value, but the absolute error value remains well under the accuracy goal of 1% of the full instrument scale ($2.4 \text{ W m}^{-2} \text{ sr}^{-1}$).

To increase the confidence level, the edition 1 unfiltered radiances of GERB-2 are validated by cross comparison with collocated and coangular Clouds and the Earth's Radiant Energy System (CERES) observations for different scene types. In addition to an overall offset between the two instruments, the intercomparisons indicate a scene-type dependency up to 4% in unfiltered radiance. Further studies are required to confirm the cause, but an insufficiently accurate characterization of the shortwave spectral response of the GERB instrument in the visible part of the spectrum is one area under further investigation.

1. Introduction

The Geostationary Earth Radiation Budget (GERB; Harries et al. 2005) instruments are the first broadband (BB) radiometers designed to operate from geostationary orbit. They are part of the Meteosat Second Generation (MSG; Schmetz et al. 2002) satellites' payload and have as a main objective the accurate observation of the diurnal cycle of the earth radiation budget at the top of the atmosphere (TOA). The on-ground processing of the GERB data is distributed between the United Kingdom and Belgium. The Rutherford Appleton Laboratory (RAL; United Kingdom) is responsible

for the calibration and the geolocation of the instrument's measurements. This generates geolocated filtered radiances that are transferred to the Royal Meteorological Institute of Belgium (RMIB) for unfiltering and conversion into fluxes. Dewitte et al. (2008) give a general overview of the GERB data processing at RMIB.

This paper describes the methodology used to determine the unfiltered shortwave radiance from the filtered radiances of the GERB-2 instrument on *MSG-1*. A companion paper (Clerbaux et al. 2008, hereafter Part II) is dedicated to the longwave radiation. The edition 1 GERB data, which are the first data released for scientific purposes, have been unfiltered with the method described in these two papers.

Compared to previous broadband instruments like the Clouds and the Earth's Radiant Energy System (CERES; Wielicki et al. 1996) or the Scanner for Ra-

Corresponding author address: Nicolas Clerbaux, Royal Meteorological Institute of Belgium, Ringlaan 3 Avenue Circulaire B-1180, Brussels, Belgium.
E-mail: nicolas.clerbaux@oma.be

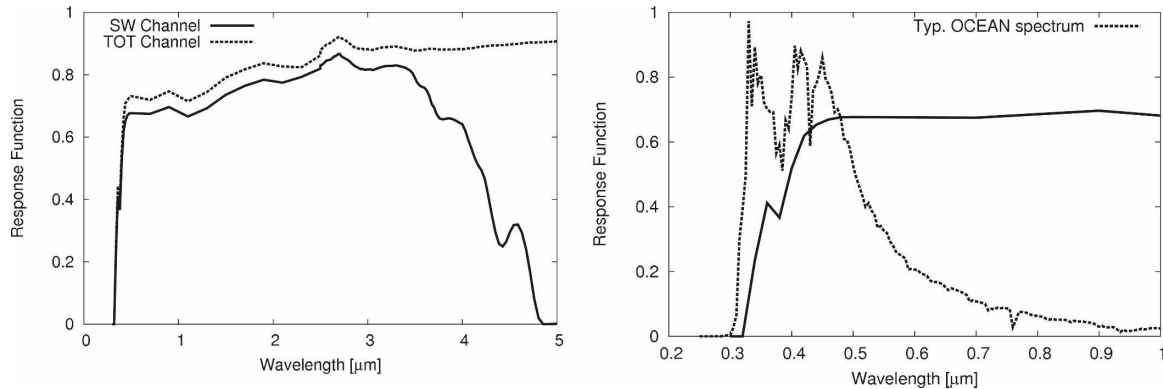


FIG. 1. (left) SW and TOT average spectral response for the GERB-2 instrument. (right) Detail of the SW spectral response at the shorter wavelength with a typical ocean spectral radiance curve $L(\lambda)$ simulated with SBDART (internal ocean model, no aerosol, SZA = 0°, VZA = 0°, and RAA = 90°).

diation Budget (ScaRaB), the GERB unfiltering is challenging because the instrument exhibits greater structure in its spectral response function. This is due to the fact that the GERB optics is composed of five mirrors: three for the telescope, one de-spin mirror to compensate for the satellite rotation, and one mirror to minimize the effect of the polarization of the radiation. The GERB instrument contains a linear array of 256 detector elements, and this is also challenging as each detector has its own spectral sensitivity. This variability is, however, not taken into account for the unfiltering algorithm for edition 1. On the other hand, the unfiltering can make use of some spectral information provided by the narrowband (NB) measurements of the Spinning Enhanced Visible and Infrared Imager (SEVIRI; Schmetz et al. 2002), the operational weather imager on board the MSG satellite series. For these reasons, various aspects of the GERB unfiltering are quite different than the unfiltering recently set up for the CERES instrument data (Loeb et al. 2001).

This first part of the paper is structured as follows. First, the spectral response curve of the GERB-2 shortwave channel is presented. Section 3 states the unfiltering problem as well as some operational constraints for the implementation of this part of the GERB data processing. Section 4 presents the radiative transfer computations that are used to parameterize the unfiltering. A comprehensive description of the unfiltering is provided in section 5. This includes the details of the method and the parameters derived for the GERB-2 instrument. Based on the radiative transfer computations, the theoretical errors introduced by the unfiltering processes are assessed in section 6. Section 7 presents the results of an intercomparison of the GERB-2 and CERES Flight Model 2 (FM2) and 3 (FM3) unfiltered radiance. This intercomparison is an overall vali-

ation of the GERB unfiltered radiance that includes the effects of the characterization of the instrument spectral response as well as the errors introduced during the unfiltering. A final discussion of the GERB shortwave channel unfiltering is provided in section 8.

2. The GERB shortwave spectral response

The GERB instrument's working principle is described in Harries et al. (2005). The preflight characterization of the instrument is performed at the Earth Observation Characterization Facility of the Imperial College, London, United Kingdom. They use detector characterization performed at Leicester University and at the U.K. National Physical Laboratory. The 256 blackened detectors of the instrument are sensitive to radiation at all wavelengths from the ultraviolet to the far infrared. The shortwave measurements are realized through a quartz filter, which only transmits wavelengths shorter than about 40 μm . Figure 1, left, shows the shortwave spectral response curve $\phi_{\text{sw}}(\lambda)$ averaged over the 256 detector elements of the GERB-2 instrument:

$$\phi_{\text{sw}}(\lambda) = \frac{1}{256} \sum_{\text{det}=1}^{256} \phi_{\text{sw}}^{\text{det}}(\lambda). \quad (1)$$

This curve is the system-level spectral response that gathers the responses of the detector, the quartz filter, the three mirrors of the reflective telescope, and the de-spin and depolarization mirrors. The effect of the quartz filter is marked by an absorption of about 7% at all the wavelengths and a cutoff for wavelengths beyond 4 μm . The lower sensitivity in the visible with respect to the near infrared is mainly due to the cumulative effect of the five silvered mirrors. Figure 1, right,

shows the sharp variation of sensitivity in the ultraviolet. A typical clear-ocean spectrum is appended to illustrate the weak sensitivity of the instrument to the shortest wavelengths of the bluest scenes. This spectral response results from the reprocessing of the data gathered during the on-ground characterization of the instrument.

3. Problem statement and constraints

For scientific use, the filtered radiance measured by the instrument L_{sw} must be converted to unfiltered reflected solar radiance L_{sol} , the radiance that would have been measured by a perfect broadband instrument [i.e., $\phi_{sw}(\lambda) = 1, \forall \lambda$] sensitive only to the reflected sunlight:

$$L_{sol} = \int L_{sol}(\lambda) d\lambda. \quad (2)$$

The measurement L_{sw} consists mainly of reflected solar radiation $L_{sw,sol}$ but also includes a small contribution from $L_{sw,th}$ because of the planetary thermal emissions from wavelengths below $5 \mu\text{m}$ and also, to a lesser extent, from wavelengths beyond $50 \mu\text{m}$ where the filter exhibits a small “leakage” transmission:

$$\begin{aligned} L_{sw} &= L_{sw,sol} + L_{sw,th}, \\ &= \int L_{sol}(\lambda)\phi_{sw}(\lambda) d\lambda + \int L_{th}(\lambda)\phi_{sw}(\lambda) d\lambda. \end{aligned} \quad (3)$$

The unfiltering factor α_{sw} for the shortwave (SW) channel is defined as the ratio

$$\alpha_{sw} = L_{sol}/L'_{sw,sol}. \quad (4)$$

The unfiltering consists of the estimation of the unfiltering factor and of the thermal contamination. Because of some ground data processing constraints (Dewitte et al. 2008), the unfiltering is realized in two steps. In a first step, the NB measurements in the 0.6-, 0.8-, and 1.6- μm channels of the SEVIRI imager are used to estimate, at the 3×3 SEVIRI pixel resolution (i.e., $9 \text{ km} \times 9 \text{ km}$ at nadir), the broadband unfiltered radiance L'_{sol} and the filtered shortwave radiance L'_{sw} . The primes (') indicate that these broadband radiances are estimated from SEVIRI through narrowband-to-broadband (NB-to-BB) conversions. The L'_{sw} is a SEVIRI estimate of the filtered radiance that would have been measured by the GERB shortwave channel and includes the solar and thermal contributions $L'_{sw} = L'_{sw,sol} + L'_{sw,th}$. The NB-to-BB conversions done during this first step use SEVIRI data, along with conversion factors based on radiance simulations for a wide variety of scenes, are totally independent of the GERB measurements. In the second step, the two SEVIRI esti-

mates are convolved with the GERB dynamic point spread function (PSF) and temporally interpolated to match the GERB measurements. The full-width at half-maximum of the GERB PSF at the subsatellite point is about 38 km (north–south) by 68 km (east–west). The GERB unfiltered solar radiance is finally obtained by multiplying the filtered measurement L_{sw} by a factor equal to the ratio of the SEVIRI estimated unfiltered and filtered radiances:

$$L_{sol} = L_{sw} \left(\frac{L'_{sol}}{L'_{sw,sol} + L'_{sw,th}} \right). \quad (5)$$

Using this formulation modeling errors should cancel for the most part, as long as the spectral response is broadband and relatively flat.

This approach is well suited to the unfiltering of BB radiances collected over a large footprint, as is the case for GERB. Indeed, most of the $38 \text{ km} \times 68 \text{ km}$ footprints contain a mixture of scenes having different unfiltering factors and this situation is taken into account with the SEVIRI finescale information.

It must be recognized that the thermal contamination $L'_{sw,th}$ is not properly taken into account in Eq. (5). Indeed, it would have been more rigorous to estimate the unfiltered GERB radiance as

$$L_{sol} = (L_{sw} - L'_{sw,th}) \left(\frac{L'_{sol}}{L'_{sw,sol}} \right), \quad (6)$$

so that the result does not depend on the absolute SEVIRI calibration that affects the L'_{sol} and $L'_{sw,sol}$ (calibration error cancels in the ratio). The unfiltering error introduced in the edition 1 GERB data because of the use of Eq. (5) instead of Eq. (6) is very small and is quantified in section 6c.

During the first step, the NB-to-BB conversions used to estimate L'_{sol} and L'_{sw} can be either theoretical (based on radiative transfer computations) or empirical (based on corresponding NB and BB measurements). However, it is critical that the unfiltered L'_{sol} and filtered L'_{sw} estimates are mutually consistent so that most of the NB-to-BB conversion error cancels in Eq. (5). In practice, a large database of spectral radiance curves is used to parameterize and test the NB-to-BB conversions. The generation of this database is described in the next section.

4. Radiative transfer computations

A large database of simulated spectral radiance curves $L_{sol}(\lambda)$ is built using version 2.4 of the Santa Barbara discrete ordinate radiative transfer (DISORT) Atmospheric Radiative Transfer (SBDART; Ricchiazzi

TABLE 1. The five geotypes used for the radiative transfer computations and the number of simulations having primary and secondary geotypes. For each geotype the surface reflectance curves from the ASTER spectral library are given in the last column.

Primary geotype	No.	Secondary geotype	No.	ASTER library surface reflectance models
Ocean	301	Ocean	301	SBDART “seawater” model
Vegetation	137	Ocean	14	Conifers, deciduous, dry grass, grass
		Vegetation	82	
		Soils	28	
		Rocks	0	
		Snow	13	
Soils	138	Ocean	14	87P3665c, 79P1530c, 87P3671c, 79P1536c, 87P3855c, 82P2230c, 87P4264c, 82P2671c, 87P4453c, 82P2695c, 87P473c, 84P3721c, 87P706c, 85P3707c, 87P707c, 85P4569c, 87P757c, 85P4663c, 87P764c, 85P5339c, 88P2535c, 86P1994c, 88P4699c, 86P4561c, 88P475c, 86P4603c, 89P1763c, 87P1087c, 89P1772c, 87P2376c, 89P1793c, 87P2410c, 89P1805c, 87P313c, 90P0142c, 87P325c, 90P128sc, 87P337c, 90P186sc, 87P3468c
		Vegetation	29	
		Soils	89	
		Rocks	0	
		Snow	6	
Rocks	150	Ocean	14	Greywa1f, limest1f, limest2f, limest3f, limest4f, limest5f, limest6f, limest7f, sandst1f, sandst2f, sandst3f, sandst4f, sandst6f, sandst7f, shale1f, shale2f, shale3f, shale4f, shale5f, shale6f, shale7f, siltst1f, siltst2f, traver1f, greywa1c, limest1c, limest2c, limest3c, limest4c, limest5c, limest6c, limest7c, sandst1c, sandst2c, sandst3c, sandst4c, sandst6c, sandst7c, shale1c, shale2c, shale3c, shale4c, shale5c, shale6c, shale7c, siltst1c, siltst2c, traver1c
		Vegetation	44	
		Soils	45	
		Rocks	45	
		Snow	9	
Snow	24	Snow	24	Coarse, medium, fine, frost

et al. 1998) model. The database contains simulations for 750 different realistic conditions for the earth surface, the atmosphere, and cloudiness.

For the generation of this database we did not try to mimic the statistics of observed scenes in the Meteosat field of view but rather to simulate as much as possible the variability in spectral signature of the scenes. For this reason, the input parameters for the radiative transfer computations are randomly selected using uniform distribution of probability over extended ranges for the parameter values instead of using climatology of observed values.

The surface is either one single or a mixture of two of the following geotypes: ocean, vegetation, soil, rocks, and snow. For the land surface, the spectral reflectance curve $\rho_{\text{surf}}(\lambda)$ of the surface is selected randomly within the Advanced Spaceborne Thermal Emission and Reflection Radiometer (ASTER) spectral library,¹ as detailed in Table 1. The rocks geotype is representative for sandy surface, which is widely present in the Meteosat field of view.

In the case of mixture, the spectral reflectance curve at the surface $\rho_{\text{surf}}(\lambda)$ is constructed as

$$\rho_{\text{surf}}(\lambda) = a_1\rho_{\text{surf},1}(\lambda) + a_2\rho_{\text{surf},2}(\lambda), \quad (7)$$

where $\rho_1(\lambda)$ and $\rho_2(\lambda)$ are the primary and secondary curves from the ASTER library. The mixing coefficients a_1 and a_2 are randomly selected between [0: 1] using a uniform distribution of probability (i.e., each value in the range has the same probability). The coefficients are then scaled in such a way that the sum $a_1 + a_2$ follows a uniform distribution of probability in the range [0.8: 1.2]. These limits allow us to reduce or boost by 20% the overall reflectance of the surface with respect to the samples stored in the ASTER library. In the case of a pure surface, the $\rho_2(\lambda)$ is taken equal to the $\rho_1(\lambda)$. Table 1 provides the numbers of simulations for the different primary and secondary geotypes. For instance, the database contains 138 simulations with soils as the primary geotype. Among these soils simulations, 14 have ocean as the secondary geotype, 29 have vegetation, 89 have soils, and 6 have snow.

For the ocean the internal “seawater” SBDART reflectance curve is used with an additional specification of the concentration of chlorophyll pigment. The pigment concentration affects the bidirectional reflectance distribution function (BRDF) of the ocean for wavelengths between 0.4 and 0.7 μm . This concentration is selected in the range [0.01: 10.0] mg m^{-3} with the base -10 logarithm of the concentration following a uniform distribution of probability in the range $[-2: 1]$. This distribution has been selected from the monthly chlorophyll concentration climatology produced by the Sea-viewing Wide Field-of-view Sensor (SeaWiFS) project (Ahmad et al. 2003).

¹ Reproduced from the ASTER Spectral Library through the courtesy of the Jet Propulsion Laboratory, California Institute of Technology, Pasadena, California, © 1999, California Institute of Technology.

The reflection of the ocean surface follows the internal BRDF implemented in SBDART. This BRDF is based on the Cox and Munk model and is dependent on the wind speed, which is selected randomly with a uniform distribution of probability in the range [1: 10] m s^{-1} . The upper limit is selected according to the global climatology of wind velocity derived from the Special Sensor Microwave Imager (SSM/I) instrument (Atlas et al. 1996). The lower limit is needed to avoid radiative transfer instabilities for wind speed below 1 m s^{-1} . The reflection of the land surfaces is isotropic as no surface BRDF is used for the simulations. The use of land surface BRDF would have been desirable, but this was recognized as out of the scope for this work as SBDART does not provide BRDF for land surfaces and BRDF measurements are not available for the ASTER library samples. The effect of not modeling the BRDF for land surface is, however, expected to be an acceptable approximation as the effect is of secondary importance and the unfiltering error is small.

For each simulation, the atmospheric profile of pressure, temperature, humidity, and ozone is selected randomly with an equal probability among the six internal profiles of SBDART. These profiles are the well-known McClatchey profiles (tropical, midlatitude summer, midlatitude winter, subarctic summer, subarctic winter) with the addition of the US62 standard U.S. atmosphere profile provided in SBDART. Boundary layer aerosols are also simulated. The type of aerosol is selected randomly with an equal probability within the following categories: none, rural, urban, oceanic, and tropospheric. The optical thickness at 0.55 μm of the aerosol is randomly selected between 0.01 and 1, with a uniform distribution of probability for the base-10 logarithm of the optical thickness. This distribution has been selected according a climatology of aerosol optical thickness retrieval from Total Ozone Mapping Spectrometer (TOMS) data inversion (King et al. 1999). Finally, the intensity of the Rayleigh scattering is multiplied by a random factor having a uniform distribution of probability in the range [0.8: 1.2]. This is implemented to enlarge the dispersion of spectrum $L(\lambda)$ over the dark oceanic scenes by altering the intensity of the atmospheric scattering by $\pm 20\%$.

Clouds are added in the simulations with a probability of 50%. For a cloudy simulation, the cloudiness can be made of up to three overlapping layers. The probabilities of these layers are 50%, 40%, and 30%, respectively, for the low-, mid-, and high-level clouds. The altitude of the low-level cloud is set randomly with a uniform distribution of probability in the range [0.5: 3.5] km, the midlevel in [4: 7] km, and the high level in [7.5: 16] km. These threshold values are selected to

match the International Satellite Cloud Climatology Project (ISCCP; Rossow and Schiffer 1991) cloud height classification. The optical thickness at 0.55 μm of a cloud layer is randomly selected between 0.3 and 300, with a uniform distribution of probability for the base-10 logarithm of the optical thickness in the range [−0.523: 2.477]. The low-level clouds are always composed of water droplets and the high-level clouds of ice particles. The phase of the intermediate layer can be either water or ice, with an equal probability. For a water cloud layer, the droplet's effective radius is selected randomly within [2: 25] μm with a uniform distribution of probability. The effective radius of ice particles is selected within [15: 128] μm also with a uniform distribution of probability.

The DISORT computations are performed using 20 streams to obtain an accurate representation of the dependency of the scene spectral signature $L(\lambda)$ with the sun–target–satellite geometry. The solar zenith angle (SZA) varies between nadir (SZA = 0°) and SZA = 80° by steps of 10°. The viewing geometry is defined by the viewing zenith angle (VZA = 0°–85° by 5° steps) and the relative azimuth angle (RAA = 0° in the forward direction w.r.t. to the incident sunlight to 180° in the backward direction by steps of 10°). The simulations cover the wavelength interval [0.25: 5.0] μm with the following spectral resolution: $\Delta\lambda = 0.005 \mu\text{m}$ over [0.25: 1.36] μm , $\Delta\lambda = 0.01 \mu\text{m}$ over [1.36: 2.5] μm , and $\Delta\lambda = 0.1 \mu\text{m}$ over [2.5: 5.0] μm . All the radiative transfer computations have been performed with the thermal emission turned off in order to simulate only the radiance $L_{\text{sol}}(\lambda)$ due to the reflection of the incoming solar radiation.

This database of spectral radiance curves is then weighted with the instrument's spectral response filters to get, for each simulation $L_{\text{sol}}(\lambda)$, the broadband and narrowband radiances:

$$\begin{aligned}
 L_{\text{sol}} &= \int_{0.25\mu\text{m}}^{5\mu\text{m}} L_{\text{sol}}(\lambda) d\lambda, \\
 L_{\text{sw,sol}} &= \int_{0.25\mu\text{m}}^{5\mu\text{m}} L_{\text{sol}}(\lambda) \phi_{\text{sw}}(\lambda) d\lambda, \\
 L_{0.6} &= \int_{0.25\mu\text{m}}^{5\mu\text{m}} L_{\text{sol}}(\lambda) \phi_{0.6}(\lambda) d\lambda, \\
 L_{0.8} &= \int_{0.25\mu\text{m}}^{5\mu\text{m}} L_{\text{sol}}(\lambda) \phi_{0.8}(\lambda) d\lambda, \quad \text{and} \\
 L_{1.6} &= \int_{0.25\mu\text{m}}^{5\mu\text{m}} L_{\text{sol}}(\lambda) \phi_{1.6}(\lambda) d\lambda, \quad (8)
 \end{aligned}$$

where $\phi_{\text{sw}}(\lambda)$ is the GERB-2 average shortwave spectral response defined by Eq. (1), and $\phi_{0.6}(\lambda)$, $\phi_{0.8}(\lambda)$, and $\phi_{1.6}(\lambda)$ are the spectral responses of the visible channels of the SEVIRI instrument on *MSG-1* [available from European Organisation for the Exploitation of Meteorological Satellites (EUMETSAT)]. In practice, all of the radiances are expressed in units of $\text{W m}^{-2} \text{sr}^{-1}$.

5. Edition 1 SW unfiltering

a. Introduction

The GERB unfiltering uses SEVIRI-based broadband estimates L'_{sol} and $L'_{\text{sw,sol}}$ obtained as the best fit of regressions on the database of simulated NB and BB radiances. These regressions are described in section 5b.

When these regressions have been applied to the early GERB and SEVIRI data it was observed that the SEVIRI-based estimate L'_{sw} exhibited systematic biases according to the actual GERB measurement L_{sw} over some parts of the Meteosat field of view (up to 10% over clear desert). These biases did not affect the unfiltering at the scale of the GERB pixels as they concerned both the L'_{sol} and L'_{sw} of the ratio in Eq. (5).

However, the biases compromise the accuracy of the enhanced spatial resolution GERB product (Dewitte et al. 2008), which combines the large-scale GERB observations L_{sw} and the finescale SEVIRI estimates L'_{sw} . For this reason an empirical adjustment to the theoretical regressions has been implemented to reduce the scene-specific biases. This adjustment is described in section 5c and is used over most of the field of view with the exception of snow and mixed ocean/land pixels, and at the terminator ($\text{SZA} > 80^\circ$). For these exceptions the theoretical regressions are used without empirical adjustment.

A specific unfiltering is implemented for the clear-ocean scene. The motivations for this specific processing as well as its description are given in section 5d.

Finally, the regression used to estimate the thermal contamination in the GERB SW channel $L'_{\text{sw,th}}$ is presented in section 5e.

These four sections, 5b–5e, form the description of the unfiltering algorithm for GERB edition 1 data.

b. Theoretical NB-to-BB regressions (nonadjusted)

The regressions estimate the broadband radiances L'_{sol} and $L'_{\text{sw,sol}}$ as a second-order polynomial regressions on the SEVIRI visible channel radiances:

$$L'_{\text{sol}} = b_0 + b_1L_{0.6} + b_2L_{0.8} + b_3L_{1.6} + b_4L_{0.6}^2 + b_5L_{0.8}L_{0.6} + b_6L_{0.8}^2 + b_7L_{1.6}L_{0.6} + b_8L_{1.6}L_{0.8} + b_9L_{1.6}^2, \quad (9)$$

$$L'_{\text{sw,sol}} = c_0 + c_1L_{0.6} + c_2L_{0.8} + c_3L_{1.6} + c_4L_{0.6}^2 + c_5L_{0.8}L_{0.6} + c_6L_{0.8}^2 + c_7L_{1.6}L_{0.6} + c_8L_{1.6}L_{0.8} + c_9L_{1.6}^2. \quad (10)$$

The regression coefficients $\{b_i\}$ and $\{c_i\}$ are estimated as a best fit on the database of spectral radiance curves for each $\text{SZA} = 0^\circ, 10^\circ, \dots, 80^\circ$. The fit is performed over the 750 earth–atmosphere conditions and over a subset of viewing geometries ($\text{VZA} = 0^\circ, 20^\circ, 40^\circ, 60^\circ$, and $\text{RAA} = 0^\circ, 60^\circ, 120^\circ, 180^\circ$). These NB-to-BB conversions are only dependent on the SZA and are not dependent on the VZA , the RAA , the surface type, or the cloudiness. Table 2 provides the coefficients $\{b_i\}$ and $\{c_i\}$ for the GERB-2 instrument, and the residual root-mean-square (RMS) error of the fit in percent. This error is evaluated with the same simulations used to generate the regression coefficients. The coefficients for $\text{SZA} = 90^\circ$ are simply cut and pasted from the $\text{SZA} = 80^\circ$ coefficients, except the independent coefficients, which are set to null $b_0 = c_0 = 0$. Before fitting Eqs. (9) and (10) on the simulations, the NB radiances $L_{0.6}$, $L_{0.8}$, and $L_{1.6}$ are randomly modified with a random noise having a Gaussian distribution with a standard deviation equal to 5% of the average radiance in the channel. This is necessary to avoid the

fits exploiting excessively slight correlations between the simulated SEVIRI channels (overfitting of the data). The 5% value is selected as representative of the calibration accuracy of the SEVIRI visible channels (Govaerts et al. 2001). When Eqs. (9) and (10) are used, parameters $\{b_i\}$ and $\{c_i\}$ are linearly interpolated in SZA .

c. Adjustment of the NB-to-BB regressions

Clerbaux et al. (2005) propose the following empirical regressions to improve the estimation of the broadband reflectances ρ'_{sol} and $\rho'_{\text{sw,sol}}$ as functions of the SEVIRI NB reflectances:

$$\begin{aligned} \rho'_{\text{sol}} = & d_0 + d_1\rho_{0.6} + d_2\rho_{0.6}^2 + d_3\rho_{0.8} + d_4\rho_{1.6} \\ & + d_5\text{SZA} + d_6\text{SGA}, \end{aligned} \quad (11)$$

$$\begin{aligned} \rho'_{\text{sw,sol}} = & e_0 + e_1\rho_{0.6} + e_2\rho_{0.6}^2 + e_3\rho_{0.8} + e_4\rho_{1.6} + e_5\text{SZA} \\ & + e_6\text{SGA}, \end{aligned} \quad (12)$$

TABLE 2. Coefficients $\{b_i\}$ and $\{c_i\}$ for the theoretical regressions [Eqs. (9) and (10)]. The $\{c_i\}$ are valid for GERB-2 SW channel. The last column gives the residual RMS error of the regressions.

SZA	b_0	b_1	b_2	b_3	b_4	b_5	b_6	b_7	b_8	b_9	RMS error $W m^{-2} sr^{-1} (\%)$
0°	14.366	4.943	6.524	-1.032	-0.033	0.021	0.079	0.280	-0.289	0.107	6.41 (4.20%)
10°	14.214	4.961	6.540	-1.123	-0.034	0.017	0.087	0.295	-0.323	0.137	6.32 (4.22%)
20°	13.597	5.000	6.481	-1.053	-0.037	0.021	0.092	0.302	-0.324	0.125	6.12 (4.28%)
30°	12.765	5.088	6.348	-0.909	-0.043	0.020	0.113	0.331	-0.358	0.103	5.77 (4.34%)
40°	11.587	5.291	5.875	0.030	-0.056	0.030	0.142	0.328	-0.294	-0.164	5.34 (4.46%)
50°	10.192	5.563	5.218	1.573	-0.077	0.058	0.167	0.291	-0.077	-0.836	4.82 (4.67%)
60°	6.829	6.721	3.695	3.481	-0.041	-0.191	0.513	0.083	-0.384	-0.091	4.84 (5.82%)
70°	4.955	6.891	3.076	5.193	-0.038	-0.415	0.969	0.325	-1.012	-0.346	3.64 (6.30%)
80°	2.730	6.563	3.931	5.523	-0.001	-0.151	0.512	-0.971	1.285	-1.903	2.16 (7.53%)
90°	0.000	6.563	3.931	5.523	-0.001	-0.151	0.512	-0.971	1.285	-1.903	—
SZA	c_0	c_1	c_2	c_3	c_4	c_5	c_6	c_7	c_8	c_9	RMS error $W m^{-2} sr^{-1} (\%)$
0°	7.129	3.177	4.351	-0.042	-0.026	0.021	0.052	0.173	-0.199	0.113	4.14 (4.19%)
10°	7.072	3.181	4.375	-0.127	-0.027	0.021	0.055	0.181	-0.220	0.137	4.06 (4.20%)
20°	6.719	3.201	4.342	-0.079	-0.030	0.025	0.059	0.186	-0.224	0.133	3.93 (4.26%)
30°	6.274	3.252	4.259	0.034	-0.035	0.026	0.072	0.206	-0.251	0.121	3.69 (4.30%)
40°	5.678	3.360	3.966	0.627	-0.044	0.036	0.091	0.209	-0.227	-0.030	3.39 (4.39%)
50°	4.993	3.511	3.560	1.604	-0.060	0.062	0.105	0.187	-0.101	-0.437	3.03 (4.55%)
60°	3.086	4.205	2.643	2.923	-0.042	-0.075	0.307	0.062	-0.290	-0.036	3.02 (5.63%)
70°	2.245	4.292	2.328	3.880	-0.054	-0.159	0.539	0.184	-0.620	-0.220	2.27 (6.09%)
80°	1.297	4.042	2.920	4.034	-0.096	0.244	0.049	-0.752	1.042	-1.291	1.35 (7.30%)
90°	0.000	4.042	2.920	4.034	-0.096	0.244	0.049	-0.752	1.042	-1.291	—

where SGA is the sun-glint angle in degrees.² The reflectances $\{\rho\}$ in Eq. (11) are the corresponding radiances L normalized by the incoming solar radiance, the cosine of SZA, and the earth–sun distance $\{\rho = L/[L_{\text{solar}} \cos(\text{SZA})/d^2]\}$. The regression coefficients $\{d_i\}$ and $\{e_i\}$ are not dependent on the SZA but are instead dependent on the surface type. The surface type is extracted from an unvarying six-classes map derived from the 1-km dataset of the International Geosphere and Biosphere Program (IGBP) classification (Townshend et al. 1994). The classes (ocean, dark vegetation, bright vegetation, dark desert, bright desert, and snow) are the same as the ones used for the GERB SW radiance-

to-flux conversion using the CERES Tropical Rainfall Measuring Mission (TRMM) angular-dependency models (Loeb et al. 2003). Table 3 gives the regression parameters $\{d_i\}$ as empirically derived by Clerbaux et al. (2005) and the RMS error in percent for the six surface types. All these values are derived from a large database of coangular SEVIRI and CERES observations (Clerbaux et al. 2005). As coefficients for snow are not provided in Clerbaux et al. (2005), they were derived as the best fit of Eq. (11) on the SBDART simulations with the snow geotype. The parameters $\{e_i\}$ are obtained as best fit on the SBDART simulations of

$$\frac{e_0 + e_1\rho_{0.6} + e_2\rho_{0.6}^2 + e_3\rho_{0.8} + e_4\rho_{1.6} + e_5\text{SZA} + e_6\text{SGA}}{d_0 + d_1\rho_{0.6} + d_2\rho_{0.6}^2 + d_3\rho_{0.8} + d_4\rho_{1.6} + d_5\text{SZA} + d_6\text{SGA}} = \frac{\rho_{\text{sw,sol}}}{\rho_{\text{sol}}}, \tag{13}$$

where the $\{\rho\}$ are the simulated reflectances. Specific fits are done for the six surface types using the appropriate geotypes in the database of simulations as indicated in Table 4. The simulations with SZA = 0°, 10°, 20°, . . . , 70°; VZA = 0°, 10°, 20°, . . . , 60°; and RAA = 0°, 10°, 30°, 60°, 90°, 120°, 150°, 170°, 180° are used. This is a selection of 504 sun–target–satellite geome-

tries among the 3249 that have been simulated. The regression coefficients $\{e_i\}$ are given in Table 3 as well as the RMS error of the fit.

The adjusted empirical regressions of Eqs. (11) and (12) replace the theoretical regressions [Eqs. (9) and (10)] over all the field of view except for snow and mixed ocean/land pixels, and at the terminator (SZA > 80°).

d. Clear-ocean unfiltering

The GERB unfiltering for the clear-ocean scene may be subject to important relative error because of the

² $\cos(\text{SGA}) = \cos(\text{VZA}) \cos(\text{SZA}) + \sin(\text{VZA}) \sin(\text{SZA}) \cos(\text{RAA})$.

TABLE 3. Coefficients $\{d_i\}$ and $\{e_i\}$ and RMS error (%) for the adjusted regressions [Eqs. (11) and (12)].

Surface	d_0	d_1	d_2	d_3	d_4	d_5	d_6	RMS
Ocean	0.015 985	0.247 134	0.004 561	0.518 540	0.015 142	0.000 129	0.000 265	5.25%
Dark vegetation	0.007 039	0.447 929	-0.018 466	0.373 205	-0.007 576	0.000 379	0.000 099	4.13%
Bright vegetation	0.006 219	0.465 640	-0.036 540	0.359 887	-0.011 129	0.000 357	0.000 169	4.64%
Dark desert	0.012 397	0.403 222	0.009 855	0.398 442	-0.028 190	0.000 207	0.000 132	4.62%
Bright desert	0.036 945	0.238 924	0.075 104	0.477 670	-0.069 874	0.000 566	0.000 097	2.69%
Snow	-0.117 821	0.301 393	-0.077 451	0.670 340	0.092 932	-0.000 197	0.000 263	2.04%
Surface	e_0	e_1	e_2	e_3	e_4	e_5	e_6	RMS
Ocean	0.011 928	0.177 863	0.000 715	0.588 210	0.026 470	0.000 125	0.000 214	0.38%
Dark vegetation	0.001 095	0.440 421	-0.023 079	0.384 094	0.009 912	0.000 381	0.000 052	0.53%
Bright vegetation	0.001 588	0.459 780	-0.041 845	0.368 241	0.006 747	0.000 357	0.000 119	0.62%
Dark desert	0.005 892	0.378 195	0.002 321	0.429 143	-0.010 994	0.000 205	0.000 088	0.56%
Bright desert	0.029 765	0.217 151	0.067 063	0.506 242	-0.052 025	0.000 567	0.000 052	0.51%
Snow	-0.107 395	0.208 925	-0.059 788	0.727 045	0.106 943	-0.000 197	0.000 226	0.24%

drop off in sensitivity of the instrument at wavelengths shorter than $0.45 \mu\text{m}$ and also because the unfiltering factor is obtained in this case as the ratio of two small quantities. Furthermore, the clear-ocean spectra $L_{\text{sol}}(\lambda)$ exhibit more dependency on angular geometry: in the backward direction the spectrum is more “blue” than in the forward direction (more “white”). Therefore, a specific unfiltering method is implemented for clear-ocean pixels. Additionally, this may ease the improvement of the clear-ocean unfiltering for subsequent editions of the GERB database. The RMIB GERB cloud detection (Ipe et al. 2004) is used to the ocean pixel as clear or cloudy.

For clear ocean, the unfiltering factor α_{sw} is estimated as a second-order regression on the inverse of the SEVIRI reflectance $\rho_{0.6}$ in the bluest channel of the instrument. The reflectance value $\rho_{0.6}$ is first clamped between minimum $\rho_{0.6,\text{min}}$ (SZA, VZA, RAA) and maximum $\rho_{0.6,\text{max}}$ (SZA, VZA, RAA) values, which are dependent on the full angular geometry. This clamping means that a value lower than the minimum is replaced by this minimum, and a value higher than the maximum is replaced by this maximum. This avoids that the highly nonlinear regression is used out of the domain of simulations. The clamped reflectance is then used in the regression

$$\alpha_{\text{sw}} = f_0(\text{SZA}, \text{VZA}, \text{RAA}) + \frac{f_1(\text{SZA}, \text{VZA}, \text{RAA})}{\rho_{0.6}} + \frac{f_2(\text{SZA}, \text{VZA}, \text{RAA})}{\rho_{0.6}^2}. \quad (14)$$

The regression parameters are derived from the 301 ocean simulations in the database, including, for the sake of robustness, the ones having cloudiness. For each angular geometry (SZA, VZA, RAA), the $\rho_{0.6,\text{min}}$ and $\rho_{0.6,\text{max}}$ are the 5% and 95% percentiles of the

simulated $\rho_{0.6}$ reflectances, and the $\{f_i\}$ are derived as the best fit of Eq. (14) over the simulations. Figure 2 illustrates the clear-ocean unfiltering for the two angular geometries: SZA = 30° , VZA = 40° , and RAA = 30° (forward observation) and RAA = 150° (backward observation). A significant difference in unfiltering factor between these two geometries is apparent in clear-sky conditions.

When Eq. (14) is used for clear-ocean unfiltering, the parameters $\{f_i\}$, $\rho_{0.6,\text{min}}$, and $\rho_{0.6,\text{max}}$ are trilinearly interpolated in SZA, VZA, and RAA. For SZA or VZA higher than 60° , the regression coefficients for 60° are used. This is needed as the radiative transfer computations sometimes provide doubtful results for grazing illumination and/or viewing angles, and in these conditions more robust results are obtained using the regression between $\rho_{0.6}$ and α_{sw} derived from the 60° simulations.

e. Thermal contamination

The small contribution of planetary thermal emission observed within the GERB shortwave filter must be estimated. This contribution is estimated as a regression on the following water vapor (WV) and infrared (IR) thermal channels of the SEVIRI instrument: WV $6.2 \mu\text{m}$, WV $7.3 \mu\text{m}$, IR $8.7 \mu\text{m}$, IR $9.7 \mu\text{m}$, IR $10.8 \mu\text{m}$,

TABLE 4. Categories and numbers of simulations used to fit Eq. (13) for the six surface types.

Surface type	Categories used	No. of simulations
Ocean	Ocean	301×504
Dark vegetation	Vegetation	137×504
Bright vegetation	Vegetation and soils	$(137 + 138) \times 504$
Dark desert	Soils and rocks	$(138 + 150) \times 504$
Bright desert	Rocks	150×504
Snow	Snow	24×504

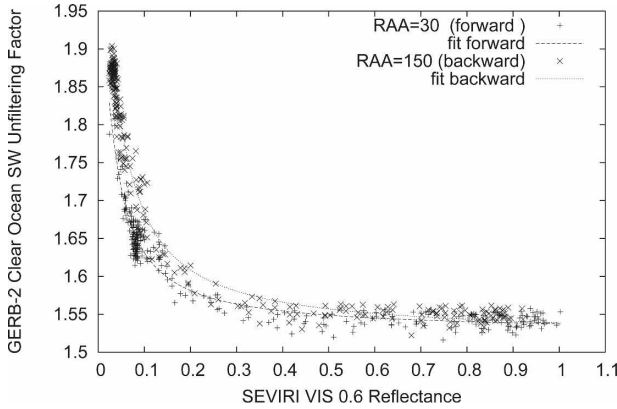


FIG. 2. Illustration of the GERB clear-ocean unfiltering with Eq. (14) fit on the SBDART simulations (dots and crosses) for two particular geometries.

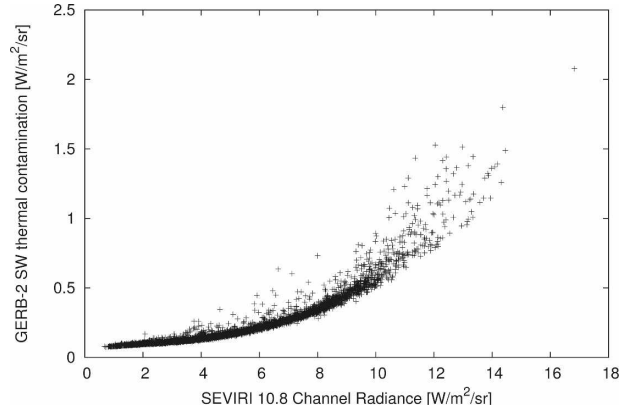


FIG. 3. Scatterplot of the thermal contamination in the GERB-2 SW channel $L_{sw,th}$ according to the SEVIRI 10.8- μm channel radiance. The dots represent the SBDART thermal simulations at $VZA = 0^\circ$.

IR 12 μm , and IR 13.4 μm (the IR 3.9- μm channel is discarded because of its daytime contamination with solar radiation). For this, radiative transfer computations in the thermal part of the spectrum are used. They are described in Part II, which treats the thermal radiation. The same database of simulations is used for the GERB longwave (LW) radiance-to-flux conversion and is described by Clerbaux et al. (2003). The simulations are performed for 4620 realistic earth-atmosphere conditions, with the atmospheric profiles extracted from

the Thermodynamic Initial Guess Retrieval, version 3 (TIGR-3) database (Chevallier et al. 2000). The spectral radiance curves $L_{th}(\lambda)$ are simulated for $VZA = 0^\circ, 5^\circ, 10^\circ, \dots, 85^\circ$ with the incoming sunlight turned off to only simulate planetary thermal radiation. Figure 3 provides an illustration of the magnitude of this contamination. A second-order polynomial regression on the seven thermal channels is selected to estimate the contamination:

$$L'_{sw,th} = g_0 + g_1L_{6.2} + g_2L_{7.3} + g_3L_{8.7} + g_4L_{9.7} + g_5L_{10.8} + g_6L_{12} + g_7L_{13.4} + g_8L_{6.2}^2 + g_9L_{7.3}L_{6.2} + g_{10}L_{7.3}^2 + g_{11}L_{8.7}L_{6.2} + g_{12}L_{8.7}L_{7.3} + \dots + g_{35}L_{13.4}^2, \quad (15)$$

where the coefficients $\{g_i\}$ of the regression are dependent on the VZA . Table 5 provides the $\{g_i\}$ values and RMS error of the regression at $VZA = 0^\circ, 25^\circ, 50^\circ$, and 75° . As for the regressions on the visible channels, and for the same reasons, the simulated NB thermal radiances are randomly modified with a random noise (5%) before the regression is fit on the simulated data.

6. Theoretical assessment of unfiltering errors

In the following sections, the different sources of error that affect the unfiltering process are addressed using radiative transfer simulations. The errors are expressed as the difference between the estimated and the actual unfiltered radiances. Thus, positive (negative) error means that the unfiltering process overestimates (underestimates) the resulting GERB unfiltered radiance.

a. Error due to the NB-to-BB regressions

Although the SEVIRI NB-to-BB theoretical regressions Eqs. (9) and (10) [or Eqs. (11) and (12) after

adjustment] are affected by about 4.5% RMS errors (Tables 2 and 3), the unfiltering error is much smaller. This assumption is verified in this section on the database of simulations for the adjusted regressions and for the specific regression in the case of clear ocean. The unadjusted regressions lead to similar kind of unfiltering errors. This is not presented here as these regressions are almost not used for the GERB unfiltering.

For each simulated spectrum $L_{sol}(\lambda)$, the broadband and the narrowband radiances L_{sol} , $L_{sw,sol}$, $L_{0.6}$, $L_{0.8}$, and $L_{1.6}$ are computed with Eqs. (8). For this simulated scene the unfiltering error due to the inaccuracy of the fits is evaluated as

$$\epsilon(\%) = 100.0 \frac{L_{sw,sol} \frac{L'_{sol}}{L'_{sw,sol}} - L_{sol}}{L_{sol}}, \quad (16)$$

where L'_{sol} and $L'_{sw,sol}$ are estimated from the simulated SEVIRI NB radiances $L_{0.6}$, $L_{0.8}$, and $L_{1.6}$ through the

TABLE 5. Regression parameters used to estimate the thermal contamination in the GERB-2 SW channel. The parameters $\{g_i\}$ are derived for $VZA = 0^\circ, 5^\circ, 10^\circ, \dots, 85^\circ$, but for illustrative purpose the table only provides values at $VZA = 0^\circ, 25^\circ, 50^\circ$, and 75° . The last row of the table gives the residual RMS error on the $L'_{sw,th}$ estimate.

Coef	SZA = 0°	SZA = 25°	SZA = 50°	SZA = 75°
g_0	0.109 891	0.107 959	0.093 887	0.046 295
g_1	0.025 456	0.014 201	-0.032 410	-0.071 040
g_2	0.021 815	0.037 101	0.083 887	0.053 752
g_3	0.199 475	0.208 667	0.220 191	0.100 299
g_4	0.085 680	0.085 725	0.079 779	0.039 715
g_5	-0.001 643	-0.004 605	-0.016 389	-0.020 494
g_6	-0.087 027	-0.091 081	-0.093 257	-0.041 257
g_7	-0.015 092	-0.011 563	0.004 937	0.041 381
g_8	-0.033 629	-0.032 856	-0.028 757	-0.050 23
g_9	0.065 353	0.064 720	0.060 050	0.131 250
g_{10}	0.004 353	0.002 067	-0.006 061	-0.088 360
g_{11}	-0.067 039	-0.095 377	-0.208 612	-0.322 644
g_{12}	0.090 746	0.118 450	0.210 737	0.173 419
g_{13}	0.221 665	0.245 670	0.329 115	0.377 443
g_{14}	-0.103 779	-0.102 799	-0.069 974	0.126 767
g_{15}	0.078 458	0.077 326	0.058 465	-0.027 887
g_{16}	0.049 733	0.045 484	0.022 712	-0.010 465
g_{17}	-0.038 698	-0.040 429	-0.036 187	-0.018 694
g_{18}	0.016 972	0.018 855	0.028 190	0.047 669
g_{19}	-0.019 584	-0.021 148	-0.028 390	-0.025 788
g_{20}	0.013 898	0.007 365	-0.020 080	-0.043 686
g_{21}	0.008 588	0.009 029	0.009 502	-0.001 727
g_{22}	-0.001 781	-0.001 242	0.000 406	-0.000 380
g_{23}	0.028 804	0.035 760	0.059 152	0.050 827
g_{24}	-0.019 544	-0.026 323	-0.046 146	-0.012 344
g_{25}	-0.151 606	-0.167 182	-0.215 467	-0.223 803
g_{26}	-0.019 853	-0.019 425	-0.015 091	0.000 102
g_{27}	0.000 119	0.001 607	0.009 319	0.020 017
g_{28}	0.026 116	0.028 850	0.035 877	0.030 283
g_{29}	-0.010 030	-0.007 708	-0.000 919	-0.012 670
g_{30}	-0.026 512	-0.028 774	-0.032 472	-0.007 240
g_{31}	-0.057 707	-0.054 134	-0.031 847	0.039 509
g_{32}	-0.002 955	-0.002 256	-0.002 014	0.000 162
g_{33}	0.001 926	0.002 106	0.002 679	0.000 372
g_{34}	0.021 315	0.020 629	0.014 089	-0.007 959
g_{35}	0.003 081	0.002 338	-0.000 449	-0.006 288
RMS error $W m^{-2} sr^{-1} (\%)$	0.0131 (5.3%)	0.0128 (5.3%)	0.0121 (5.3%)	0.0159 (8.3%)

NB-to-BB regressions. Figure 4 shows the scatterplots of the unfiltering error ϵ versus L_{sol} for the six surface types and for a given sun–target–satellite geometry (SZA = 30°, VZA = 30°, RAA = 90°). The figure also provides the unfiltering bias (the average of the unfiltering error) and RMS error:

$$\text{bias} = \frac{1}{N} \sum_{i=1}^N \epsilon_i, \quad (17)$$

$$\text{rms} = \sqrt{\frac{1}{N} \sum_{i=1}^N (\epsilon_i - \text{bias})^2}, \quad (18)$$

where the summation is done on the simulations that belong to a particular scene type. This figure shows the

unfiltering error when the adjusted regressions are used. The figure shows that the unfiltering does not introduce significant bias in cloudy conditions and is affected by a small RMS error of less than the half percent. For the clear-sky simulations, up to a 2% unfiltering error is observed over some surface types. However, for this particular geometry, the bias and the RMS error for each of the six surface types are limited to 0.5% and 0.8%, respectively.

Similar scatterplots, biases, and RMS errors are obtained at the other sun–target–satellite geometries. Table 6 provides the unfiltering bias and RMS error for the six surface types and the clear and cloudy conditions averaged over the following (sub)set of 14 sun–target–satellite geometries:

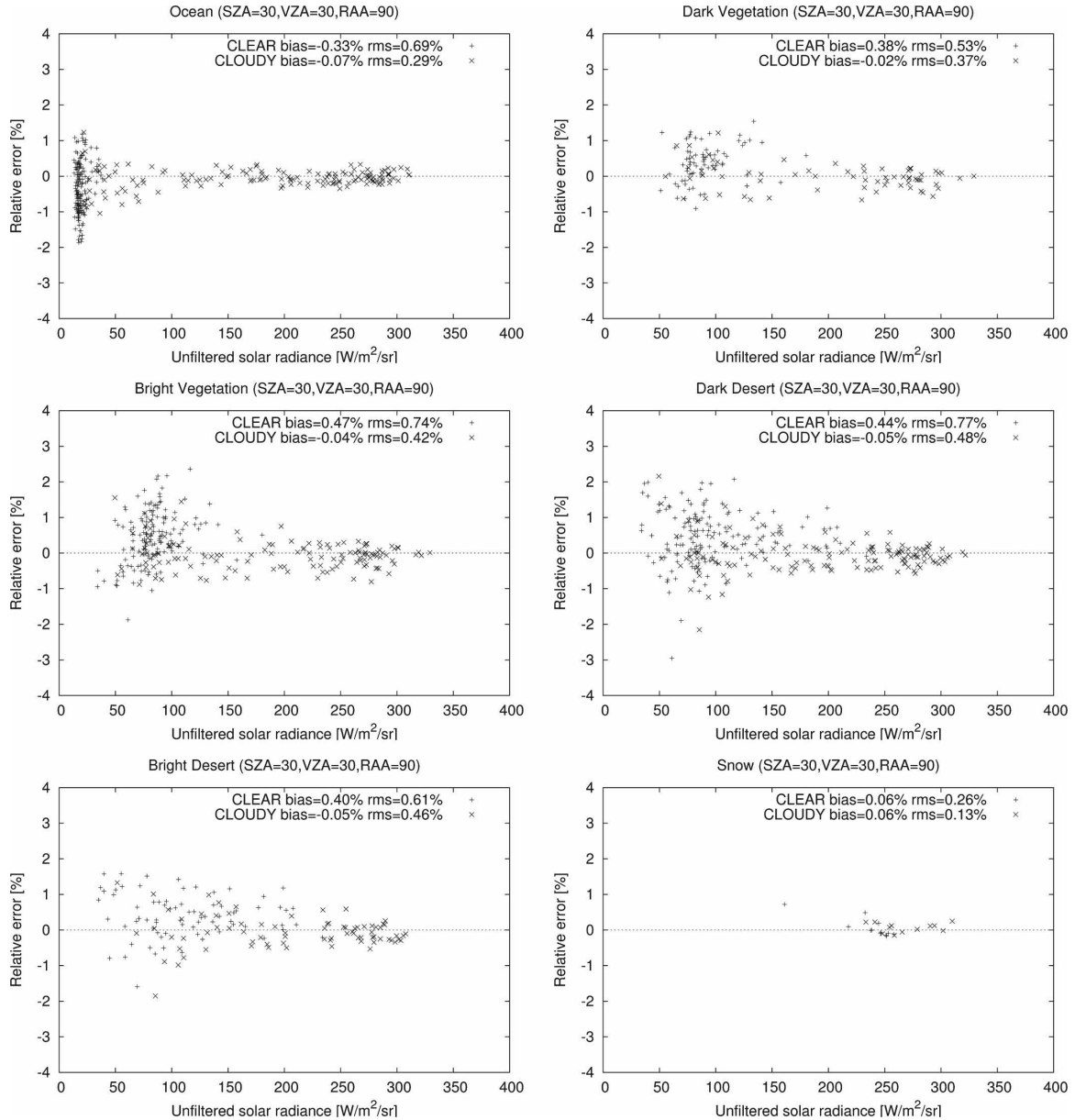


FIG. 4. Scatterplots of unfiltering error ϵ vs the broadband radiance L_{sol} for the adjusted regressions at the $\text{SZ} = 30^\circ$, $\text{VZ} = 30^\circ$, and $\text{RA} = 90^\circ$ geometry. The scatterplots are built from the SBDART simulations classified in six classes of surface type and for clear (+) and cloudy (x) conditions.

$$\begin{aligned}
 (\text{SZ}, \text{VZ}, \text{RA}) = & (0, 0, 90), (0, 30, 90), (0, 60, 90), (30, 0, 90), (30, 30, 20), (30, 30, 90), (30, 30, 160), (30, 60, 20), \\
 & (30, 60, 90), (30, 60, 160), (60, 0, 90), (60, 30, 20), (60, 30, 90), (60, 30, 160). \quad (19)
 \end{aligned}$$

When the SBDART simulations for all the geometries are considered together the table shows that the biases and RMS errors are less than 0.2% and 0.8% for the different surface types and cloudiness, respectively. However, for all the scenes the bias is dependent on the geometry. The second part of Table 6 indicates the bi-

ases and RMS errors for the “worst” geometry in the set defined at Eq. (19). This worst geometry is the one that presents the highest absolute value of the bias ($|\text{bias}|$). For these worst cases, the biases lie between -0.85% and $+0.88\%$ and are positive in clear and negative in cloudy conditions.

TABLE 6. Average bias (%) and RMS (%) of the unfiltering error ϵ for various scene types. The unfiltering is realized with the adjusted regressions except for the clear ocean for which the specify regression is used. The first column of numbers provides the errors when all the geometries are put together, while the last column is for the “worst” geometry. This geometry is given in parentheses (SZA, VZA, RAA).

Scene type		Radiative transfer model	All geometries together bias (%) / RMS (%)	Worst geometry bias (%) / RMS (%) (SZA, VZA, RAA)
Ocean	Clear	SBDART	-0.12/1.16	0.45/0.99 (00,00,090)
	Clear	6S	0.38/1.08	1.22/1.33 (00,00,090)
	Clear-continental	6S	-0.27/0.76	1.17/1.35 (00,00,090)
	Clear-maritime	6S	0.66/0.52	1.22/0.20 (00,00,090)
	Clear-urban	6S	1.15/1.00	2.08/1.43 (00,00,090)
	Clear-desert	6S	1.07/0.56	1.41/0.17 (00,00,090)
	Clear-biomass	6S	-0.69/0.96	-1.30/0.75 (00,00,090)
Dark vegetation	Cloudy	SBDART	0.03/0.33	-0.85/0.76 (00,00,090)
	Clear	SBDART	0.13/0.60	0.48/0.53 (00,60,090)
	Clear	6S	0.41/0.44	0.71/0.31 (00,60,090)
Bright vegetation	Cloudy	SBDART	-0.01/0.43	-0.60/0.42 (00,00,090)
	Clear	SBDART	0.18/0.79	0.53/0.66 (00,60,090)
	Clear	6S	0.37/0.62	0.76/0.43 (00,60,090)
Dark desert	Cloudy	SBDART	-0.04/0.49	-0.73/0.50 (00,00,090)
	Clear	SBDART	0.19/0.79	0.52/0.77 (00,60,090)
	Clear	6S	0.50/0.60	0.85/0.64 (00,60,090)
Bright desert	Cloudy	SBDART	-0.05/0.51	-0.69/0.59 (00,00,090)
	Clear	SBDART	0.20/0.66	0.63/0.76 (00,60,090)
	Clear	6S	0.39/0.52	0.88/0.69 (00,60,090)
Snow	Cloudy	SBDART	-0.04/0.49	-0.62/0.57 (00,00,090)
	Clear	SBDART	0.06/0.25	-0.25/0.30 (00,00,090)
	Cloudy	SBDART	0.05/0.19	-0.25/0.17 (00,00,090)

The previous set of geometries, and then also the result given in Table 6, does not contain grazing solar and/or viewing geometries. Figure 5 provides a more complete analysis of the dependency of the unfiltering errors (bias and RMS error) as a function of the SZA and VZA angles. Figures 5a–d provide separate analysis according to the scene types, with different VZA and RAA considered together. Figure 5a shows a systematic decrease of the bias at increasing SZA for the different surface types in clear-sky conditions. At high solar zenith angle, this clear-sky bias reaches $\sim -0.8\%$. Figure 5c shows the opposite dependency for cloudy conditions, but to a smaller extent. Figures 5e–h provide the SZA dependency for the different angles of observation VZA, with the different surface types and RAA considered together. Figure 5e shows that the decreases of the bias observed in clear-sky conditions in Fig. 5a are due to the simulations at high VZA. For nadir observation (VZA $\sim 0^\circ$) the clear-sky bias does not present significant SZA dependency. In summary of Fig. 5, the GERB unfiltering method has a propensity to underestimate the unfiltered radiance (i) in clear-sky conditions at grazing observation and illumination angles (bias of about -2% for SZA $\sim 70^\circ$ and VZA $\sim 70^\circ$) and (ii) in cloudy conditions at nadir sun and observation (bias of about -0.5% for SZA $\sim 0^\circ$ and VZA $\sim 0^\circ$).

For more confidence, the error introduced into the unfiltering has been assessed on an independent set of spectral radiance curves $L_{\text{sol}}(\lambda)$ generated at Imperial College using the second simulation of the satellite signal in the solar spectrum (6S; Vermote et al. 1997) radiative transfer model. The database contains only clear-sky simulations performed for the same set of 14 geometries given in Eq. (19). The land surface reflectance curves are extracted from the ASTER library. For the ocean simulations, the internal 6S model is used for the three wind speeds (1, 5, and 10 m s^{-1}), five aerosol types, and six aerosol optical thickness (0.1, 0.2, 0.4, 0.6, 0.8, and 1).

Figure 6 shows the scatterplots of the unfiltering error for the 6S simulations at the (SZA = 30° , VZA = 30° , RAA = 90°) geometry. The scatterplots present patterns similar to the ones of Fig. 4.

The average and worst-case bias and RMS error for this second set of simulations are given in Table 6. As for the SBDART simulations, the unfiltering errors for spectra simulated with 6S present positive biases for clear-sky conditions. For all the geometries together, the bias lies between 0.37% and 0.5% according to the surface type. For the worst geometry (also a sun at the zenith) the bias lies between 0.71% and 1.22%. The 6S simulations are used to quantify the unfiltering error introduced by tropospheric aerosol over clear-ocean

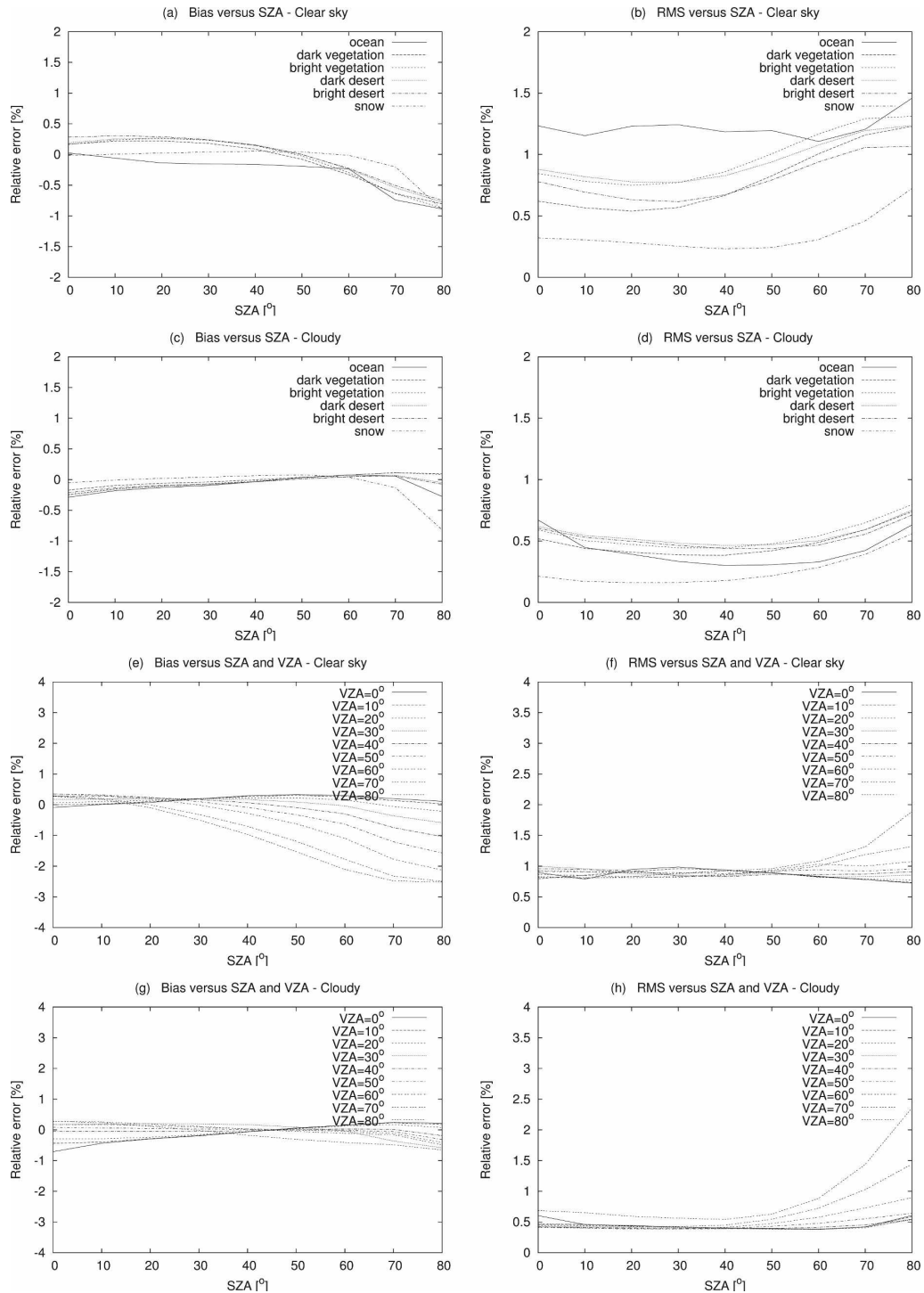


FIG. 5. SZA dependency of the (left) bias and (right) RMS error for clear and cloudy conditions. In (a)–(d) the analysis is done for the different surface types (all VZA together), while the analysis in (e)–(h) is for different VZA (all surface types together).

surface. For the worst geometry the error remains less than $|\epsilon| < 2.08\%$ (urban aerosol). For all the geometries together, the biases are dependent on the type of aerosol. Negative biases are observed for continental

(-0.31%) and biomass (-0.74%) aerosol. Maritime (0.63%), urban (1.06%), and desert (1.03%) present positive biases.

Finally, Fig. 7 shows the scatterplots of ϵ separately

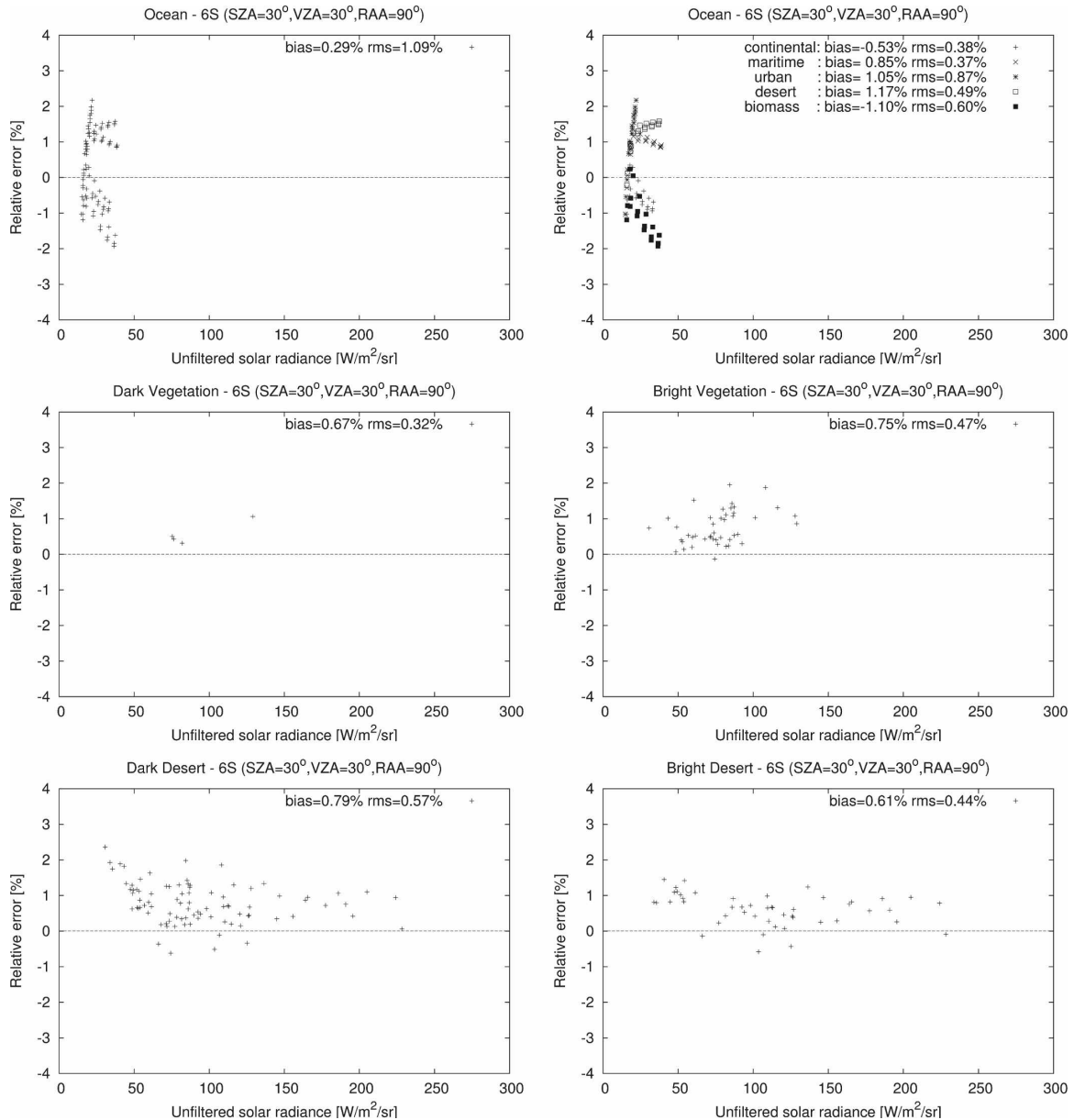


FIG. 6. Scatterplots of unfiltering error ϵ vs the broadband radiance L_{sol} for the adjusted regressions at the $\text{SZ} = 30^\circ$, $\text{VZA} = 30^\circ$, and $\text{RAA} = 90^\circ$ geometry. The scatterplots are built from the 6S clear-sky simulations classified in five classes of surface type (no snow scenes are simulated). The upper-right scatterplot shows the unfiltering errors according to the aerosol type over clear ocean.

for the 14 geometries of Eq. (19). The figure also provides the biases and RMS errors. In general the clusters of simulations are correctly centered with respect to the $\epsilon = 0\%$ line. This bias lies between 0.07% and 0.72%. The RMS error stays relatively constant at $\sim 0.8\%$ for these geometries except for the upper-left plot ($\text{SZ} = 0^\circ$, $\text{VZA} = 0^\circ$, $\text{RAA} = 90^\circ$) where an error of up to 4% is observed. These higher unfiltering errors correspond to sun-glint conditions over calm clear ocean. At this geometry, the bias for the clear-ocean simulations is

2.75% for the simulations with wind speed at 1 m s^{-1} , 0.89 at 5 m s^{-1} , and only 0.02% at 10 m s^{-1}

b. Error in the estimated thermal contamination

The estimation of the thermal contamination in the GERB-2 SW channel $L_{\text{sw,th}}$ is realized with Eq. (15). Figure 8 shows the scatterplot of the error on the $L_{\text{sw,th}}$ quantity according to the NB radiance in the $10.8\text{-}\mu\text{m}$ SEVIRI channel for the 4620 thermal simulations and for the $\text{VZA} = 0^\circ$ angle. The figure shows that the error

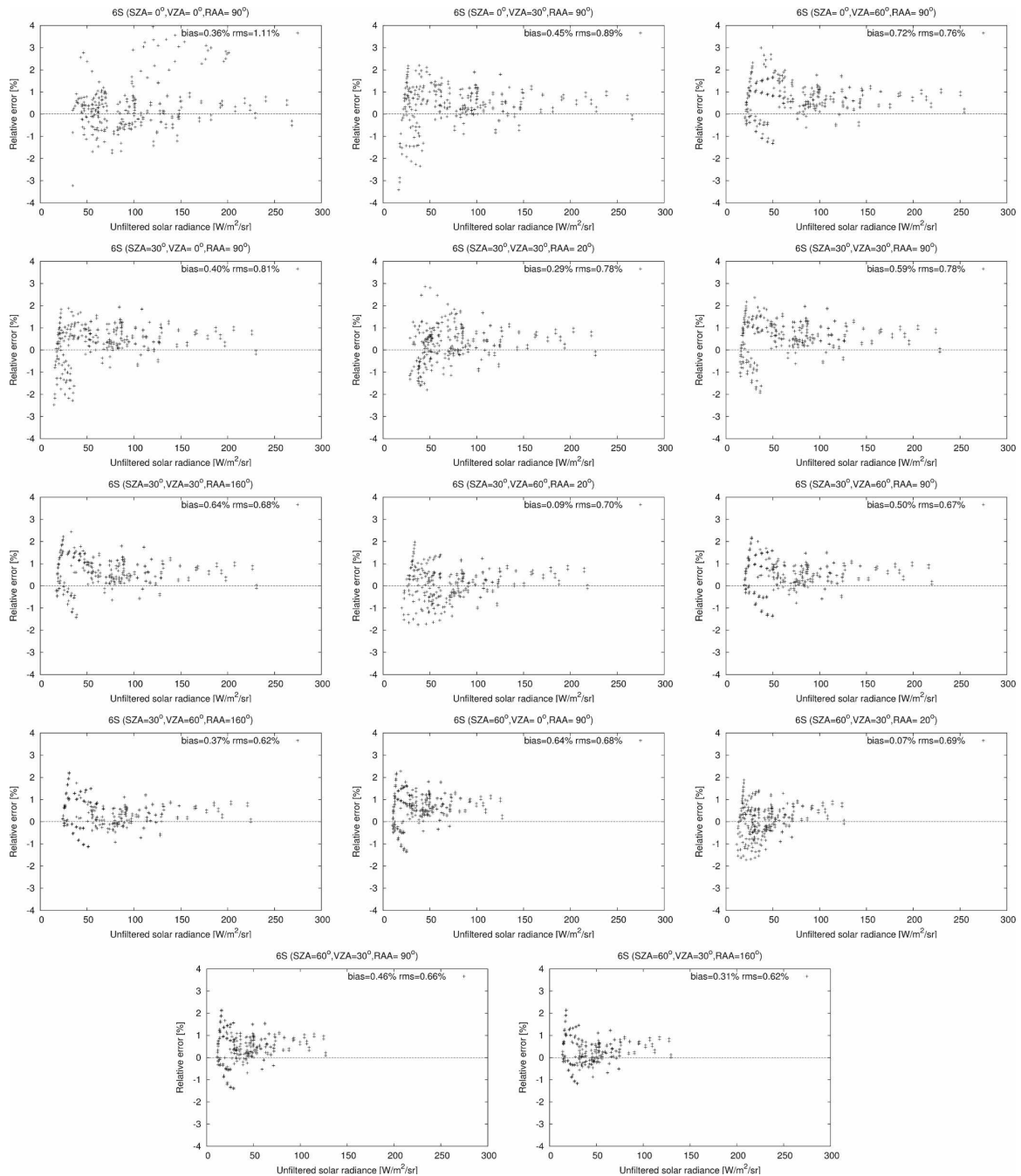


FIG. 7. Scatterplots of unfiltering error ϵ vs the broadband radiance L_{sol} for the adjusted regressions of the 14 geometries listed in Eq. (19). Each symbol represents one 6S simulation.

on the contamination is in general very small. Over the database of thermal simulations, the RMS error is only $0.03 W m^{-2} sr^{-1}$. However, some LW simulations present higher errors, which can reach values of up to $-0.28 W m^{-2} sr^{-1}$. As this error does not depend on the intensity of the solar radiance, it is expressed in $W m^{-2} sr^{-1}$.

In nighttime conditions, the accuracy of this estimation can also be assessed on actual GERB and SEVIRI data. Figure 9 shows the scatterplot of the estimated contamination $L_{sw,th}$ versus the GERB measurement L_{sw} for $SZA > 110^\circ$ conditions between 0400 and 0500 UTC 8 February 2007. Each point corresponds to average data over $10^\circ \times 10^\circ$ latitude and longitude box.

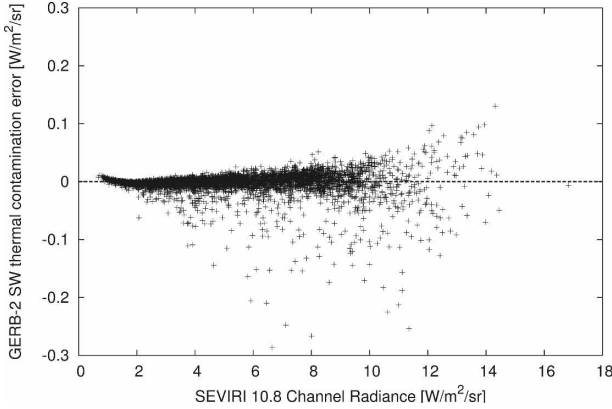


FIG. 8. Scatterplot of the error on the estimated thermal contamination in the GERB-2 SW channel $L_{sw,th}$ according to the SEVIRI 10.8- μm channel radiance. The dots represent the SB-DART thermal simulations at $VZA = 0^\circ$.

The figure shows a good correlation although the SEVIRI-based estimation appears overestimated by about $0.07 \text{ W m}^{-2} \text{ sr}^{-1}$. This can be due to inaccuracy in the regression but can also result of the spectral response definition of the SW channel between 3 and 5 μm or beyond 50 μm (leakage of the filter). The overestimation can be the result of the in-fly determination of the instrument offset and the possible effect of stray light on this determination.

c. Subtraction of the thermal contamination

As stated in section 3, the implementation of the edition 1 GERB data processing does not properly compensate for the thermal contamination in the GERB SW measurement. This introduces a small error ϵ , which is the difference between Eqs. (6) and (5):

$$\epsilon = L'_{sol} \frac{L_{sw} - L'_{sw,th}}{L'_{sw,sol}} - L'_{sol} \frac{L_{sw}}{L'_{sw,sol} + L'_{sw,th}}. \quad (20)$$

Let $\beta = L_{sol}/L'_{sol}$ be the ratio between the actual and NB-to-BB estimated shortwave radiance. Equation (20) reduces to

$$\epsilon = L'_{sol}(1 - \beta) \frac{L'_{sw,th}}{L'_{sw,sol}}. \quad (21)$$

The highest errors are expected for warm scenes for which the SW NB-to-BB regressions are inaccurate ($\beta \neq 1$). Figure 10 shows the distribution of the error given by Eq. (21) evaluated on actual GERB and SEVIRI data from 0730 UTC 20 September 2006. This error is always small ($\epsilon \ll 0.2 \text{ W m}^{-2} \text{ sr}^{-1}$). However, the relative error can be significant over warm clear-ocean scenes at low solar elevation angle. Relative er-

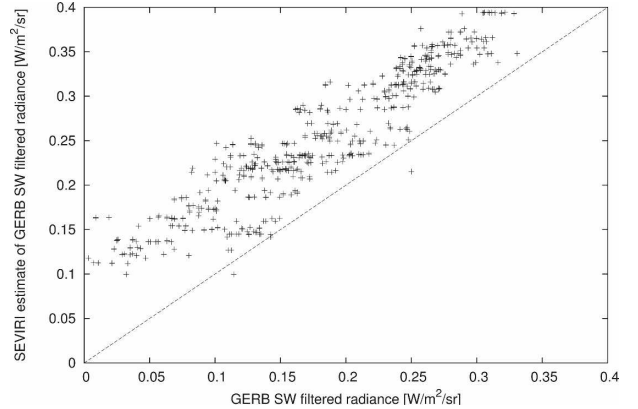


FIG. 9. Nighttime scatterplot of the estimated thermal contamination in the GERB-2 SW channel $L_{sw,th}$ according to the GERB measurement. Each point in the figure corresponds to average data over $10^\circ \times 10^\circ$ latitude and longitude box.

rors of up to 4% are observed on the unfiltered radiance L_{sol} .

d. Sensitivity to SEVIRI absolute calibration

The impact of the SEVIRI instrument's absolute calibration on the GERB unfiltering must be assessed. The calibration of the SEVIRI solar channels will impact the estimation of the unfiltering factor α_{sw} , while the calibration of the thermal channel will affect the estimation of $L_{sw,th}$. To assess this, the effects of changing the SEVIRI channel calibration by -5% , 0% , and $+5\%$ have been simulated.

From the unfiltering point of view, the worst case occurs when some solar channels have a $+5\%$ change while others have -5% change. An overestimation of the unfiltering factor by 0.8% is observed for $+5\%$ in the 0.6- μm channel and -5% in the 0.8- and 1.6- μm channels.

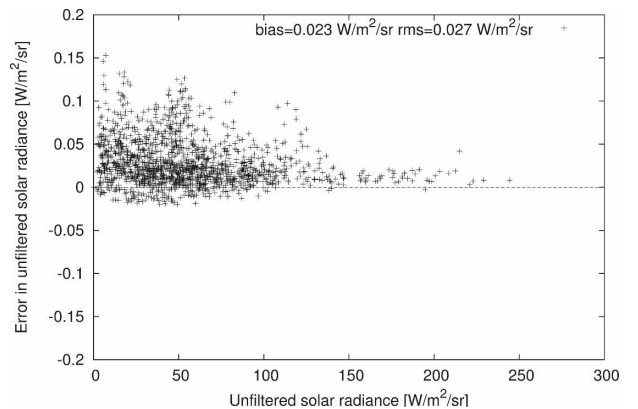


FIG. 10. Error introduced on the solar radiance because of the incorrect subtraction of the thermal contamination in the SW channel.

The impact on the estimated thermal contamination is observed when all the channels are changed by +5%, and this introduces an overestimation of the contamination having the same magnitude. As the contamination can reach up to $1.5 \text{ W m}^{-2} \text{ sr}^{-1}$ for very warm scenes (Fig. 3), the effect on the unfiltered solar radiance is $\epsilon = 0.075 \text{ W m}^{-2} \text{ sr}^{-1}$.

e. Pixel-to-pixel variability

Each line in the GERB level 1.5 image is obtained with a distinct detector. The unfiltering implemented for the first edition of the GERB level 2 products is based on the average spectral response. We do not expect, and there is no indication of, significant difference in spectral response of the different detector elements. The quantification of this is not obvious, as the accuracy of the instrumental characterization of the detector spectral response is not precise enough. The study (Mlynchak et al. 2006) of the pixel-to-pixel variability by cross comparison with CERES radiance at the GERB detector level is an ongoing activity. It should also be noted that the current implementation of the ground processing software does not allow detector level unfiltering.

7. Intercomparison with the CERES unfiltered radiances

Cross comparisons between GERB edition 1 and CERES data have been made for two weeks in 2004 (21–27 June and 11–17 December). These periods have been selected as covering special observation campaigns when the CERES FM2 instrument has been operated in the “GERB” scanning mode to optimize the number of coangular observations. The latest editions of the CERES Single Scanner Footprint (SSF) data for the FM2 and FM3 instruments have been used: edition 2B for FM2 and edition 1B for FM3. The correction for the CERES quartz filter darkening has been performed to obtain the corresponding “revision 1” data.

For each GERB averaged rectified geolocated (ARG) pixel SW unfiltered radiance, the average corresponding CERES value within the pixel is evaluated by averaging all the CERES data with observation time within 170 s of the ARG time integration period and with the angle between the GERB and CERES directions of observation less than 5° . Additional criteria are $\text{SZA} < 80^\circ$ and $\text{GERB VZA} < 65^\circ$. The number of coangular observations for FM2 (FM3) is 39 512 (8171). The value of the special GERB scanning mode employed by FM2 is obvious in the extra matches obtained with this instrument.

TABLE 7. GERB and CERES SW intercomparison summary. Average GERB/CERES ratio and associated uncertainty from Eq. (23).

	GERB/ (CERES FM2)	GERB/ (CERES FM3)
All scenes together		
June	1.058 ± 0.005	1.070 ± 0.013
December	1.048 ± 0.005	1.075 ± 0.006
Overcast condition (cloud cover = 100% and $\tau > 7.4$)		
June	1.041 ± 0.013	1.042 ± 0.017
December	1.032 ± 0.005	1.050 ± 0.017
Clear-sky condition (cloud cover = 0%)		
Ocean	1.144 ± 0.043	1.084 ± 0.052
Dark vegetation	1.070 ± 0.017	1.089 ± 0.039
Bright vegetation	1.062 ± 0.010	1.086 ± 0.013
Dark desert	1.073 ± 0.019	1.101 ± 0.035
Bright desert	1.059 ± 0.006	1.082 ± 0.012

For the intercomparisons, the ratio of the mean GERB and CERES SW unfiltered is evaluated on a daily basis:

$$m_{\text{day}} = \frac{\langle v_{\text{gerb}} \rangle}{\langle v_{\text{ceres}} \rangle}. \tag{22}$$

The daily basis is adopted because 24 h are needed for these polar-orbiting instruments to cover the whole Meteosat disk (with the night pass discarded). Note that although a day of data is used, the matches are limited to the time of the CERES overpass for each particular region. The daily ratios m_{day} are expected to be stable day after day because the sampling is the same. For a 7-day period, the best estimate of the GERB/CERES ratio m and the associated uncertainty is therefore

$$m = \langle m_{\text{day}} \rangle \pm \frac{3\sigma(m_{\text{day}})}{\sqrt{N}}, \tag{23}$$

where $\sigma(m_{\text{day}})$ is the standard deviation of the daily values around the mean value $\langle m_{\text{day}} \rangle$, and N is the number of daily values (typically seven). The factor 3 in Eq. (23) is used to have a likelihood of 99% on the m interval.

Table 7 summarizes the intercomparison results for all scenes together, overcast conditions, clear-sky conditions, and finally for each of the different surface types under clear-sky conditions. The scene identification used to identify these scenes is the GERB scene identification (Ipe et al. 2004). Some scene dependence is seen in the radiance comparison. The SW agreement (in terms of the ratio) between GERB and CERES is better for bright scenes than for dark scenes. When the clear-ocean scene is discarded, the scene dependence in the SW radiance intercomparison is limited to about

4%. This is a little more than the sum of the stated accuracy of the two datasets, which is 1% for CERES and 2.25% for GERB edition 1 (Russell 2006).

These comparisons used CERES edition 2 revision 1 data. For a clear-sky ocean scene comparison, the ocean correction was applied to the CERES data; for other comparisons the all-sky correction was applied. To gain more confidence in the scene dependence of the comparison, we plan to repeat the comparison when edition 3 of the CERES data is available in which the correction appropriate for each scene type will have been applied within the CERES processing.

8. Summary

The new GERB instruments measure SW and total (TOT) filtered radiances that must be converted to unfiltered reflected sunlight and emitted thermal radiances—and later the corresponding fluxes—for scientific applications. The unfiltering method for the GERB-2 edition 1 shortwave channel is presented. The method takes advantage of the spectral information available from the SEVIRI multispectral weather imaging radiometer, which is on the same satellite. The unfiltering is realized through a set of regressions that link the unfiltering factor to the NB solar channels of SEVIRI. The regression coefficients are derived from a large database of radiative transfer computations.

The theoretical error analysis shows that the instantaneous unfiltering error is limited, with an RMS error of less than 1.0%. A small bias can be introduced during the unfiltering according to the surface type, the cloudiness, and the sun–earth–satellite geometry. This bias remains below 1% with two exceptions: the clear-sky scenes for geometries having simultaneously high solar and viewing zenith angle, and also some simulated clear-ocean scenes with high aerosol load. In these cases biases of more than 2% are reported by the theoretical assessment.

The thermal contamination in the GERB SW channel is estimated with a regression of the SEVIRI thermal channel radiances. This estimation is very accurate with an RMS error of only $0.03 \text{ W m}^{-2} \text{ sr}^{-1}$. Nighttime validation on actual GERB and SEVIRI data exhibits, however, a higher error of about $0.07 \text{ W m}^{-2} \text{ sr}^{-1}$. Although this does not significantly affect the GERB products, the source of this discrepancy is under investigation.

The intercomparisons between GERB and CERES unfiltered SW radiances result in larger differences than would be expected from the stated accuracies of the two datasets (2.25% for GERB and 1% for CERES) and the uncertainty in the comparison method

(between 0.5 for FM2 and 1.3% for FM3 for all scenes). A marked scene dependence in the difference is also seen, with agreement best for the bright conditions of completely overcast cases and worst for the darkest and bluest scenes of clear ocean. While there are many possible causes of this discrepancy, none of which can yet be ruled out, the accuracy of the SW portion of the GERB spectral response is under further investigation and will include new measurements on the instrument flight spare detector. In addition, a study to investigate the use of the CERES unfiltering database on the GERB data using the current GERB spectral response is under way; this will allow the effects of a different theoretical framework and method to be separated from the effects of the instrument spectral response.

Acknowledgments. The authors are grateful to the Atmospheric Sciences Data Center at NASA Langley Research Center for providing the CERES data used for validation of this work.

REFERENCES

- Ahmad, Z., J. R. Herman, A. P. Vasilkov, M. Tzortziou, G. B. Mitchell, and M. Kahru, 2003: Seasonal variation of UV radiation in the ocean under clear and cloudy conditions. *Ultraviolet Ground- and Space-Based Measurements, Models, and Effects III*, J. R. Slusser, J. R. Herman, and W. Gao, Eds., International Society for Optical Engineering (SPIE Proceedings, Vol. 5156), 63–73.
- Atlas, R., R. Hoffman, S. Bloom, J. Jusem, and J. Ardizzone, 1996: A multiyear global surface wind velocity dataset using SSM/I wind observations. *Bull. Amer. Meteor. Soc.*, **77**, 869–882.
- Chevallier, F., A. Chédin, F. Chéruy, and J. J. Morcrette, 2000: TIGR-like atmospheric-profile databases for accurate radiative-flux computation. *Quart. J. Roy. Meteor. Soc.*, **126**, 777–785.
- Clerbaux, N., S. Dewitte, L. Gonzalez, C. Bertrand, B. Nicula, and A. Ipe, 2003: Outgoing longwave flux estimation: Improvement of angular modelling using spectral information. *Remote Sens. Environ.*, **85**, 389–395.
- , C. Bertrand, D. Caprion, B. Depaeppe, S. Dewitte, L. Gonzalez, and A. Ipe, 2005: Narrowband-to-broadband conversions for SEVIRI. *Proc. 2005 EUMETSAT Meteorological Satellite Conference*, Dubrovnik, Croatia, European Organisation for the Exploitation of Meteorological Satellites, 351–357.
- , S. Dewitte, C. Bertrand, D. Caprion, B. Depaeppe, L. Gonzalez, A. Ipe, and J. Russell, 2008: Unfiltering of the Geostationary Earth Radiation Budget (GERB) data. Part II: Longwave radiation. *J. Atmos. Oceanic Technol.*, **25**, 1106–1117.
- Dewitte, S., L. Gonzalez, N. Clerbaux, A. Ipe, and C. Bertrand, 2008: The geostationary earth radiation budget edition 1 data processing algorithms. *Adv. Space Res.*, **41**, 1906–1913.
- Govaerts, Y., A. Arriaga, and J. Schmetz, 2001: Operation vicarious calibration of the MSG/SEVIRI solar channels. *Adv. Space Res.*, **28**, 21–30.
- Harries, J. E., and Coauthors, 2005: The Geostationary Earth Radiation Budget Project. *Bull. Amer. Meteor. Soc.*, **86**, 945–960.

- Ipe, A., N. Clerbaux, C. Bertrand, S. Dewitte, and L. Gonzalez, 2004: Validation and homogenisation of cloud optical depth and cloud fraction retrievals for GERB/SEVIRI scene identification using meteosat-7 data. *Atmos. Res.*, **72**, 17–37.
- King, M., Y. Kaufman, D. Tanr, and T. Nakajima, 1999: Remote sensing of tropospheric aerosols from space: Past, present, and future. *Bull. Amer. Meteor. Soc.*, **80**, 2229–2260.
- Loeb, N., K. Priestley, D. Kratz, E. Geier, R. Green, B. Wielicki, P. Hinton, and S. Nolan, 2001: Determination of unfiltered radiances from the clouds and the earth's radiant energy system instrument. *J. Appl. Meteor.*, **40**, 822–835.
- , N. Smith, S. Kato, W. Miller, S. Gupta, P. Minnis, and B. Wielicki, 2003: Angular distribution models for top-of-atmosphere radiative flux estimation from the clouds and the earth's radiant energy system instrument on the tropical rainfall measuring mission satellite. Part I: Methodology. *J. Appl. Meteor.*, **42**, 240–265.
- Mlynczak, P., G. Smith, P. Szewczy, J. Russell, H. Harries, S. Dewitte, and N. Clerbaux, 2006: Comparisons of GERB and CERES measurements. Preprints, *12th Conf. on Atmospheric Radiation*, Madison, WI, Amer. Meteor. Soc., 13.1. [Available online at <http://ams.confex.com/ams/pdfpapers/111906.pdf>.]
- Ricchiazzi, P., S. Yang, C. Gautier, and D. Sowle, 1998: SBDART: A research and teaching software tool for plane-parallel radiative transfer in the earth's atmosphere. *Bull. Amer. Meteor. Soc.*, **79**, 2101–2114.
- Rossow, W., and R. Schiffer, 1991: ISCCP cloud data products. *Bull. Amer. Meteor. Soc.*, **72**, 2–20.
- Russell, J., 2006: Quality summary for GERB Edition-1 L2 ARG. Reference Doc., Imperial College, London, United Kingdom, 19 pp.
- Schmetz, J., P. Pili, S. Tjemkes, D. Just, J. Kerkmann, S. Rota, and A. Ratier, 2002: An introduction to Meteosat Second Generation (MSG). *Bull. Amer. Meteor. Soc.*, **83**, 977–992.
- Townshend, J., C. Justice, D. Skole, J.-P. Malingreau, J. Cihlar, P. Teillet, F. Sadowski, and S. Ruttenberg, 1994: The 1-km AVHRR global data set: Needs of the international geosphere biosphere program. *Int. J. Remote Sens.*, **15**, 3319–3332.
- Vermote, E., D. Tanre, J. Deuze, M. Herman, and J.-J. Morcrette, 1997: Second simulation of the satellite signal in the solar spectrum, 6S: An overview. *IEEE Trans. Geosci. Remote Sens.*, **35**, 675–686.
- Wielicki, B. A., B. R. Barkstrom, E. F. Harrison, R. B. Lee III, G. L. Smith, and J. E. Cooper, 1996: Clouds and the Earth's Radiant Energy System (CERES): An earth observing system experiment. *Bull. Amer. Meteor. Soc.*, **77**, 853–868.